



Microseismic event location using global optimization algorithms: An integrated and automated workflow



Soledad R. Lagos*, Danilo R. Velis*

Universidad Nacional de La Plata, Facultad de Ciencias Astronómicas y Geofísicas, Argentina
CONICET, Argentina

ARTICLE INFO

Article history:

Received 27 December 2016
Received in revised form 21 June 2017
Accepted 4 December 2017
Available online 8 December 2017

Keywords:

Microseismic monitoring
Optimization
Location

ABSTRACT

We perform the location of microseismic events generated in hydraulic fracturing monitoring scenarios using two global optimization techniques: Very Fast Simulated Annealing (VFSA) and Particle Swarm Optimization (PSO), and compare them against the classical grid search (GS). To this end, we present an integrated and optimized workflow that concatenates into an automated bash script the different steps that lead to the microseismic events location from raw 3C data. First, we carry out the automatic detection, denoising and identification of the P- and S-waves. Secondly, we estimate their corresponding backazimuths using polarization information, and propose a simple energy-based criterion to automatically decide which is the most reliable estimate. Finally, after taking proper care of the size of the search space using the backazimuth information, we perform the location using the aforementioned algorithms for 2D and 3D usual scenarios of hydraulic fracturing processes. We assess the impact of restricting the search space and show the advantages of using either VFSA or PSO over GS to attain significant speed-ups.

© 2017 Elsevier B.V. All rights reserved.

1. Introduction

One of the main objectives of microseismic monitoring is to locate events associated to hydraulic fracturing processes, which has numerous applications in unconventional reservoir characterization and exploitation (Kendall et al., 2011). During these procedures, thousands of microseismic events could occur distributed around fracture networks that depend on the reservoir conditions and the fracturing plan. Accurately determining the position of each event helps understanding the shapes and sizes of the induced fractures and to estimate the dimensions of the stimulated rock (Van der Baan et al., 2013), which is of great interest not only to appraise the completion and the fracture treatment (Cipolla et al., 2011), but also for avoiding potential natural hazards such as water reservoir contamination. Thus, being able to automatically perform the detection and location of microseismic events by processing the records in real time (Zimmer and Jin, 2011; Lagos et al., 2014) could help in taking rapid decisions in the field, which are of paramount importance. It is

the importance of these tasks what motivated us to develop efficient algorithms capable of expeditiously process large amounts of data.

We considered the different steps that lead to the location of microseismic sources following a *pick-based* approach, which involve the accurate determination of the phases arrival times. As described by Warpinski (2009), the general procedure is not different from standard earthquake seismology principles. Broadly speaking, it consists in detecting the phase arrivals on the microseismic records, determining the arrival times of P- and S-waves and locating the events, i.e. finding the coordinates of the microseismic source using *a priori* estimated formation velocities. From the difference between P- and S-waves arrival times only the distance to the microseismic source can be estimated (Eisner et al., 2009). Hence a pick-based approach requires the determination of the direction where the energy comes from (backazimuth) prior to event location (Maxwell et al., 2010). This can be done by studying the particle motion associated with the incoming phases (Eisner et al., 2010).

In practice, we perform the detection of both P- and S-waves and the determination of their corresponding arrival times by means of a pattern recognition strategy that employs VFSA to find high coherence values along hyperbolic time windows throughout the 3C input traces (Velis et al., 2015). The waveforms within this time window are subsequently denoised by means of a reduced-rank singular value decomposition as described by Velis et al. (2015). We obtain the backazimuth from the motion polarization analysis of

* Corresponding authors at: Facultad de Ciencias Astronómicas y Geofísicas, Paseo del Bosque s/n, La Plata 1900, Argentina.

E-mail addresses: slagos@fcaglp.unlp.edu.ar (S.R. Lagos), velis@fcaglp.unlp.edu.ar (D.R. Velis).

both P- and S-waves and propose a simple energy-based strategy to decide which backazimuth estimation is most reliable. Finally, we automatically locate the microseismic events by solving a non-linear optimization problem that takes advantage of the backazimuth information for restricting the search space. We concatenate all these steps into a single bash script that can be used to process raw 3C microseismic data in a quasi-supervised way.

As for the location problem, which constitutes the main objective of this work, we solve it using VFSA (Ingber, 1989) and PSO (Kennedy and Eberhart, 1995; Shaw and Srivasta, 2007), thoroughly analyze their performances from the point of view of their computational efficiency and compare them against the classical GS (Lagos et al., 2014), which is used in most commercial software. To this end, we consider 2D and 3D problems given by the typical acquisition geometries on fracking scenarios, which consist of a set of receivers deployed within vertical or nearly vertical monitoring wells, on account of cost limitations and well spacing (Eisner et al., 2009). The main results indicate that VFSA was up to 8 times faster than GS, and 2 times faster than PSO for 3D fracking scenarios. In the 2D case, the speed-ups with respect to GS were about 4 and 2 for VFSA and PSO, respectively.

2. Methods

Fig. 1 outlines the main processes of the automated workflow that lead to the location of a microseismic event in either 2D or 3D scenarios. The integrated workflow requires the input of the velocity model, the number of receivers and their positions, an initial search space and the observed 3C microseismic data. For simplicity, we omitted some intermediate steps related to the input/output handling and various associated processes. In the next sections we describe in detail every relevant process, including best practice strategies and limitations when dealing with low S/N ratios and large datasets.

2.1. Detection and denoising

In this work we use a technique developed by Velis et al. (2015) consisting in a two-step process in which an event is first detected and then denoised. The detection, which includes the arrival-time picking, is carried out by means of a pattern recognition strategy that searches for high coherence values within hyperbolic time windows that embrace all the traces simultaneously. The search is performed via VFSA which gives the method a high degree of efficiency. Based on the analysis that the authors made for different measures of signal coherence, we choose the *stack energy* defined by

$$G_{se} = \frac{1}{3M} \sum_{i=1}^M \left[(\bar{s}_i^c)^2 + (\bar{s}_i^y)^2 + (\bar{s}_i^z)^2 \right], \quad (1)$$

where \bar{s}_i^c is the i -th sample of the normalized mean trace along the trial hyperbola (c indicates component) and M is the number of samples of the search window. The output includes a set of parameters that define the optimum hyperbola (i.e. arrival times) that leads to maximum signal coherence. Since all channels are processed simultaneously, the variation of the arrival times as a function of depth is smooth, which is very convenient for a more reliable estimation of the backazimuth from the S-wave polarization. The method also includes a synchronizing step to take care of phase arrivals not aligned along a hyperbola, as it would be the case for heterogeneous velocity media (Velis et al., 2015).

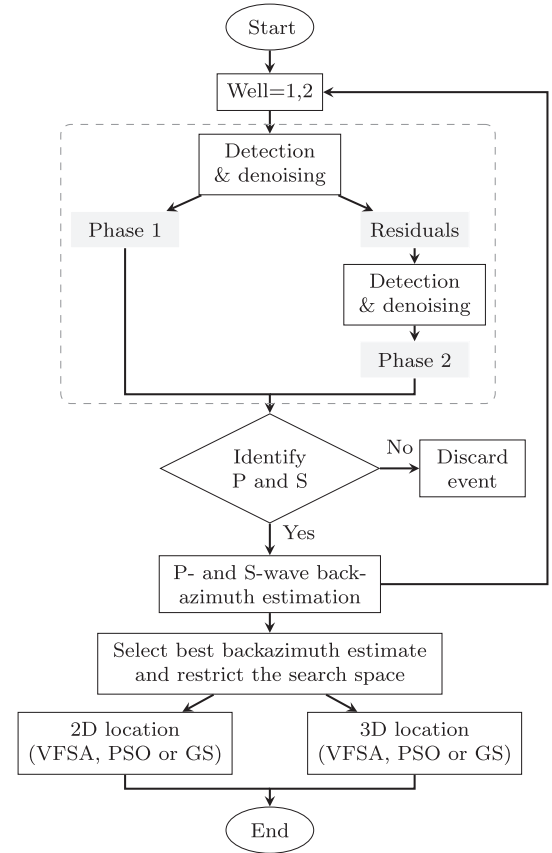


Fig. 1. Integrated flowchart describing the main processes leading to a microseismic event location.

Denoising is performed by means of a reduced-rank singular value decomposition (SVD) of the data within the hyperbolic time window that contains the detected phase (Velis et al., 2015):

$$S_q = \sum_{i=1}^q \sigma_i \mathbf{u}_i \mathbf{v}_i^T, \quad q < N \quad (2)$$

where N is the number of traces, S_q is a $M \times N$ matrix of rank q containing the phase waveform approximation, and \mathbf{u}_i , \mathbf{v}_i and σ_i ($i = 1, N$) are the eigenvectors and singular values, respectively, of the SVD of S_q with $q = N$. In practice, we found that good results are obtained with $q = 1$ or 2 , ensuring that all waveforms are similar after the reduced-rank approximation.

Together with the arrival times of the detected phase, the algorithm provides an indicator of its relative energy:

$$R = \frac{E}{\bar{E}_n}, \quad (3)$$

where E is the energy of the phase arrival and \bar{E}_n is the mean energy of the noise. Both quantities are computed within hyperbolic time windows of size $M \times N$.

Given a 3C microseismic dataset, the maximization of G_{se} leads to the detection of the one phase whose stack energy is the highest. Hence, in order to find both P- and S-waves, the procedure needs to be applied twice, considering the residuals from the first step (original data minus first detected and denoised phase) as the input for the second one. By comparing their arrival times, it is possible to determine which phase each detected wave corresponds to. We include additional controls to avoid false detections, such as in the

case of low S/N ratio scenarios where the maximization of G_{se} may lead to spurious or residual detections.

Fig. 2 illustrates the two-step detection and denoising procedure. In the first panel the S-wave can be clearly identified, but the P-wave is barely recognizable due to the low S/N ratio. After the first step, the S-wave arrival has been detected and denoised appropriately (Fig. 2b). Fig. 2c shows the results after applying the detection and denoising to the residual (data in Fig. 2a minus data in Fig. 2b), where the P-wave phase arrival is clearly seen.

2.2. Backazimuth estimation

Polarization of P- and S-waves are known to have different behaviors from which the propagation direction can be estimated (Jurkevics, 1988; Eisner et al., 2009). For isotropic media, their polarizations are parallel and perpendicular to the propagation direction, respectively. On the one hand, estimating the backazimuth is quite simpler for P-waves than for S-waves. On the other hand, since the S/N ratio is usually higher for S- than for P-waves, it is specially useful to obtain the backazimuth by means of the former (Eisner et al., 2009).

For the polarization analysis we follow the method proposed by Jurkevics (1988). Broadly speaking, it involves the calculation of the covariance matrix of the three components of motion of either the P- or the S-wave and the determination of its eigenvalues and eigenvectors. The polarization vector, which in the case of the P-wave corresponds to the propagation direction, is estimated from the eigenvector associated with the largest eigenvalue.

In the case of the S-wave, we proceed as proposed by Eisner et al. (2009) for a linear borehole array in an isotropic medium. The slowness vector \mathbf{p} , which is equal to the propagation direction divided by the velocity, should satisfy the Eikonal equation. Thus, $\mathbf{p} \cdot \mathbf{p} = V_S^{-2}$, where V_S is the S-wave velocity. Moreover, the polarization vector \mathbf{e} is perpendicular to the slowness vector, i.e. $\mathbf{p} \cdot \mathbf{e} = 0$, and the derivative of the S-wave arrival time with respect to the borehole direction gives the projection of \mathbf{p} in this direction: $p_z = dt_S/dz$.

Some provisos must be taken into account. First, the ray direction cannot be determined if the S-wave polarization is in the borehole direction. Furthermore, there are two slowness vectors that satisfy the above relations (Eisner et al., 2009). In practice, one should select the one that points approximately towards the treatment well.

We will refer to the real backazimuth of a microseismic event as θ and to its estimation as $\hat{\theta}$. Whether we find $\hat{\theta}$ using P- or S-wave polarization analysis, we have one solution for each of n usable receivers. Based on these estimations a unique backazimuth is determined. To this end, we assume that they are normally distributed and that the mean value is the “real” backazimuth (Han, 2010; Aster et al., 2005). Since n is small, we rely on the Student’s t -distribution to better estimate the mean (recall that the corresponding Student’s t -probability

density function approaches a normal distribution when n goes to infinity). Then, the new variable

$$t = \frac{\tilde{\theta} - \bar{\theta}}{s/\sqrt{n}} \quad (4)$$

follows a Student’s t -distribution with $n - 1$ degrees of freedom, where $\bar{\theta}$ is the backazimuth obtained from a single trace, and $\hat{\theta}$ and s are the sample mean and standard deviation, respectively. We obtain the mean value of t by maximizing its density function and update $\bar{\theta}$ and s accordingly. Since the backazimuth estimations are highly sensitive to noise, outliers are very likely to occur. For this reason, those backazimuth estimates that differ from the updated mean value in more than one standard deviation are removed. This process can be iteratively applied taking proper care not to overly reduce the sample size.

Depending on the relative positions of sources and receivers, the amplitudes of P- and S-waves can be remarkably different. After several tests we observed that the errors are larger for $\hat{\theta}_P$ than for $\hat{\theta}_S$ for low S/N ratios because the noise impact is larger for the former, as explained above. Contrarily, for relatively low noise levels, the errors are larger for $\hat{\theta}_S$, even though the amplitudes of S-waves are much larger than the amplitudes of the P-waves. This means that if both phases had the same S/N ratio, the backazimuth estimates obtained from the P-wave would be more reliable than those obtained from the S-wave. On the other hand, for moderate to low S/N ratios, the use of S-waves would be advisable. Moreover, as explained above, it is not possible to obtain $\hat{\theta}_S$ when the S-wave polarization is in or near the direction of the well (in our case, vertical). Therefore, we propose the use of the energy indicator R (Eq. (3)), which can be calculated for each phase and component individually, to automatically decide which phase is more reliable to estimate the backazimuth. In a nutshell, $\hat{\theta}_P$ should be used in those cases where R is larger for P- than for S-waves ($R_P > R_S$), or at least larger than both its horizontal components simultaneously, i.e. $R_P > R_S^x$ and $R_P > R_S^y$. Otherwise, $\hat{\theta}_S$ should be used.

Lastly, given the well-known 180° ambiguity (illustrated in Fig. 3) that arises when working in an azimuthally isotropic velocity medium, and since automation is our goal, we assume that the waves are coming from the stimulated regions. This assumption is valid when there is actually no other fluid displacements or no stress relaxation associated with previous stages is occurring simultaneously (Eisner et al., 2009), which could be misinterpreted as events of the current stage. Hence, we consider only the events that occurred within the “expected region”. In particular, we define this area by a 110° angle range, which is wide enough to encompass most possible backazimuths. Those arrivals that come from outside that region are not considered and should be individually evaluated to find out

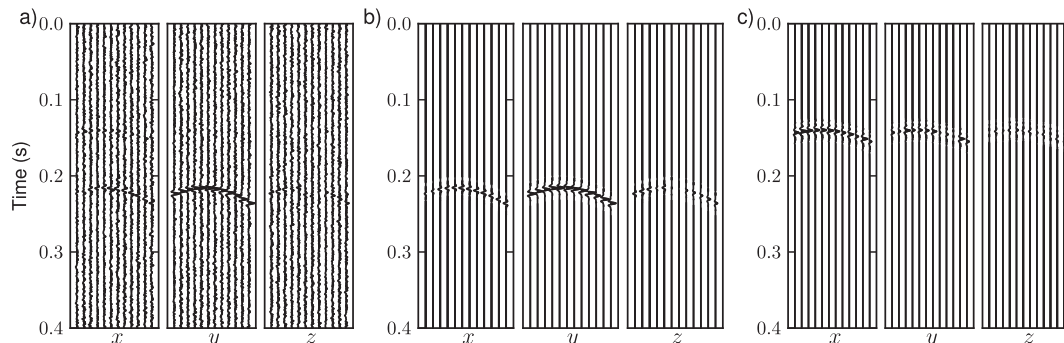


Fig. 2. a) Synthetic record; b) and c) results after the first and second steps of the detection and denoising algorithm.

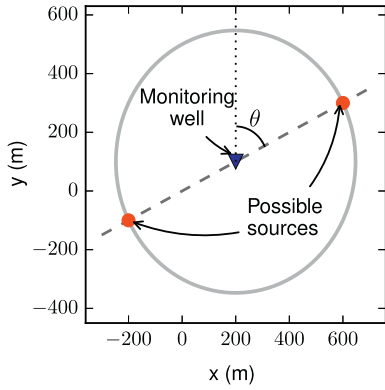


Fig. 3. Representation of the 180° ambiguity.

whether they correspond to events of interest occurring out of the treatment region.

2.3. Location

The pick-based approach we follow for the microseismic event location requires the determination of the differences between the S- and P-waves arrival times (Lagos et al., 2014). In practice we minimize the cost function

$$\phi(x_s, y_s, z_s) = \left[\frac{1}{N_c} \sum_{i=1}^{N_c} (\Delta t_i - \Delta t_i^{obs})^2 \right]^{1/2}, \quad (5)$$

where $N_c = 3 \times N$ is the number of channels, and Δt_i and Δt_i^{obs} are the modeled and observed time differences between the S- and P-waves arrivals. This non-linear function can be minimized via a variety of methods. As we stated earlier, in this work we minimize this cost function by means of VFSA (Ingber, 1989) and PSO (Shaw and Srivasta, 2007), which proved to be much more efficient than standard methods such as grid search (GS) (Lagos et al., 2014).

For the GS implementation we use regular meshes with elements of side h embracing a predefined search space. The cost function is evaluated at each node in each iteration. For the first iteration, we set $h = 50$ m for the whole search space. After each iteration, we set $h = h/2$ and update the search space around the current global minimum. The iteration is repeated until a stop criterion is reached. In order to facilitate the statistical analysis described in the Results and discussion section, the lowest left corner of the mesh in the first iteration is randomly selected within an element of size h .

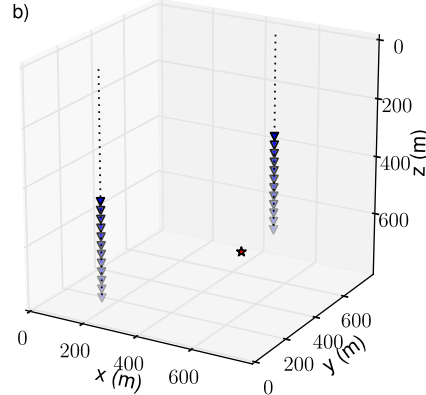
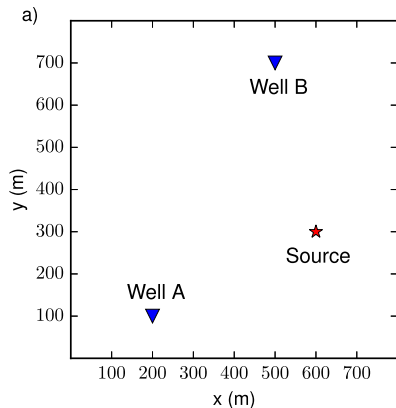


Fig. 4. Acquisition geometry.

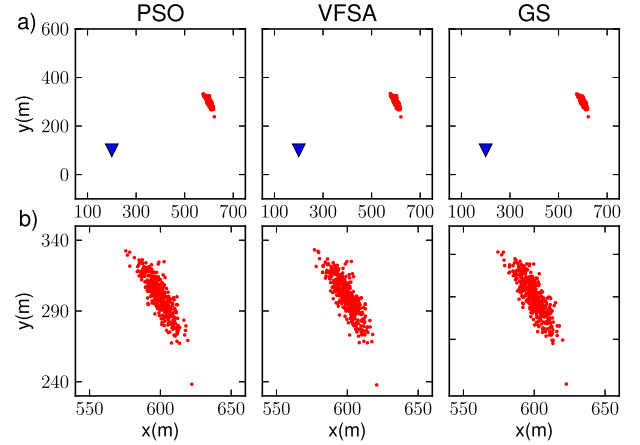


Fig. 5. 2D location example: a) Estimated source positions (400 realizations). b) Zoomed-in plots.

PSO basically consists in moving a swarm of particles through the search space. The model unknowns (microseismic source coordinates) are represented by the positions of the particles, which are iteratively updated taking advantage of both previous individual experience and social knowledge. A more extensive description of the algorithm and its implementation can be found in Appendix A. VFSA is implemented as described by Velis (1998).

3. Results and discussion

We now focus on the efficiency of the optimization methods from a statistical point of view. We consider two different acquisition geometries or models. The first model includes a single vertical monitoring well (Well A) with a 12-receiver array starting at the coordinates (200, 100, 350) m with a vertical spacing of 30 m, in a subsurface given by a homogeneous and isotropic half-space with $V_p = 3500$ m/s and $V_s = 2200$ m/s. This constitutes a 2D location problem where x_s and y_s are replaced by the horizontal distance from the receiver once $\hat{\theta}$ has been estimated. The second model includes a second monitoring well (Well B) with a 12-receivers array starting at the coordinates (500, 700, 350) m and with the same vertical spacing. In this case we perform a 3D location, since the backazimuth information is not used to reduce the number of unknowns. We consider a source at $(x_s, y_s, z_s) = (600, 300, 600)$ m assuming that the source mechanism is a shear fracture on the plane (x, z) with a slip in the $-x$ direction. Fig. 4 illustrates the spatial distribution of the described wells and the fictitious source.

Table 1
2D location example: errors in the estimated coordinates, uncertainties and number of cost function evaluations (mean values after 400 realizations and 100 repetitions).

	Target misfit: 0.5×10^{-3} s			Target misfit: 1.0×10^{-3} s		
	PSO	VFSA	GS	PSO	VFSA	GS
ε_x (m)	5.9	5.9	6.0	6.2	6.3	6.3
ε_y (m)	10.6	10.7	10.7	10.7	10.7	10.7
ε_z (m)	5.6	6.2	7.5	10.7	12.0	14.1
u_x (m)	1.1	1.2	1.4	2.1	2.4	2.6
u_y (m)	0.6	0.6	0.7	1.2	1.3	1.4
u_z (m)	3.8	4.0	3.9	7.1	7.4	7.5
N_E	248 ± 11	170 ± 8	552 ± 15	190 ± 7	122 ± 5	463 ± 29
Speed-up	2.2	3.3	1	2.4	3.8	1

The propagated signal is a Ricker wavelet with a peak frequency of 100 Hz. For statistical purposes, we generated a set of 400 synthetic records with the same source but different noise realizations. Since analyzing the effects of different focal mechanisms on the detection and location processing is out of the scope of this work, we considered the same type of source for every record. The data is contaminated with band-limited Gaussian noise with $S/N = 3$, which yields a S/N ratio for the P-wave close to 1. The S/N ratio is computed as the quotient between the maximum signal (considering both P- and S-waves) and noise amplitudes.

We test the performances of the algorithms for two different target misfits: 0.5 ms and 1 ms. Given that most service companies offer sampling intervals of 0.25 ms or smaller (Eisner et al., 2010), the expected misfits that we set are consistent with an error in the arrival time determination of 2 and 4 samples, respectively. For the sake of efficiency, we set the search space as small as possible being careful not to preclude regions of potential sources. The iterative process in all cases is stopped when the cost function satisfies a predefined target misfit or a maximum of 10,000 cost function evaluations is reached.

3.1. 2D location example

We performed the 2D location of the microseismic source for each of the 400 noise realizations with the three optimization algorithms. For statistical purposes, in each case we repeated the optimization 100 times using different seeds. The results of a single run are depicted in Fig. 5. As expected, the largest uncertainty is associated

with the backazimuth estimation, which is evident from the resulting arch-shaped cloud of events that seem to keep the distance from the well.

Table 1 summarizes the results after averaging the 100 repetitions for each of the 400 realizations for two different target misfits. The absolute errors in the estimated coordinates (ε_x , ε_y and ε_z) are very similar for the three algorithms and fall within the usual observational errors for microseismic event location in single vertical array scenarios (Eisner et al., 2009). The quantities named u_x , u_y and u_z represent the uncertainties in the estimated source coordinates due to the stochastic nature of the algorithms. Given a certain target misfit, these uncertainties are similar for the three algorithms and in every case they represent a small proportion of the absolute error in the source coordinates. It follows from the above that the only difference regarding the performances of the three optimization algorithms relies on their computational efficiency, which is the most important result in what our work is concerned. Naturally, the mean number of cost function evaluations (N_E) needed to reach a solution increases when we demand a smaller misfit. It is clear that both PSO and VFSA require significantly smaller number of cost function evaluations than GS, leading to speed-ups that go from 2 for PSO to 4 for VFSA, approximately.

3.2. 3D location example

Fig. 6 shows the results of the 3D location corresponding to one out of the 100 repetitions for the 400 realizations. Table 2 summarizes the averaged results for the same two target misfits we set in the 2D location example. Again, positioning errors are within the usual values, but smaller than in the 2D case, since the uncertainty introduced by the backazimuth is no longer present. As expected, location errors are larger for the vertical component (Eisner et al., 2009). As in the previous section, the 100 repetitions of the optimization with the different algorithms allow us to evaluate the uncertainties on the source positioning regardless of the noise realizations effects. For a given target misfit, these uncertainties are very similar for the three algorithms. Since for 3D location the algorithms explore a 3D search space, the mean N_E is larger than in the 2D case. The biggest change is observed for GS, which requires about 4 and 8 times the number of cost function evaluations required by PSO and VFSA, respectively.

3.3. Search space restriction

In the case of the 3D location, the information provided by the two monitoring wells make it unnecessary to obtain the backazimuth from the polarization analysis. However, we can take advantage of the backazimuth estimates for restricting the search space and attain higher computational efficiency. We assume that the actual source position is somewhere close to the intersection between the two directions given by the backazimuths estimated

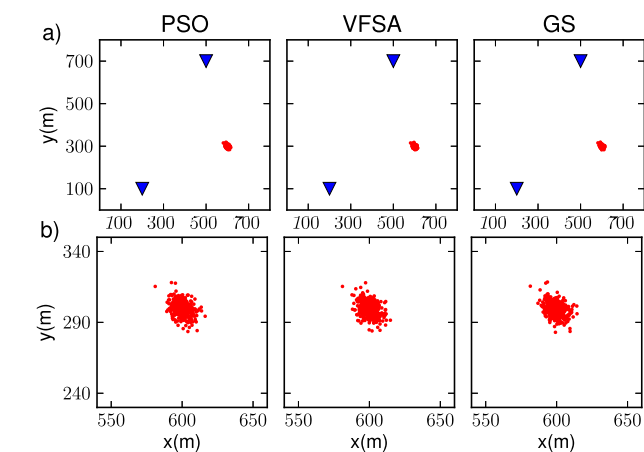


Fig. 6. 3D location example: a) Estimated source positions (400 realizations). b) Zoomed-in plots.

Table 2
3D location example: errors in the estimated coordinates, uncertainties and number of cost function evaluations (mean values after 400 realizations and 100 repetitions).

	Target misfit: 0.5×10^{-3} s			Target misfit: 1.0×10^{-3} s		
	PSO	VFSA	GS	PSO	VFSA	GS
ε_x (m)	3.7	3.8	3.8	4.5	4.9	4.9
ε_y (m)	3.8	3.9	3.9	4.6	5.0	5.0
ε_z (m)	4.8	5.3	5.6	8.6	10.3	10.6
u_x (m)	1.5	1.7	1.7	2.8	3.1	3.0
u_y (m)	1.5	1.7	1.7	2.7	3.1	3.0
u_z (m)	3.1	3.3	3.2	5.8	6.5	6.4
N_E	444 ± 16	243 ± 13	1910 ± 182	328 ± 129	148 ± 7	1165 ± 225
Speed-up	4.3	7.9	1	3.5	7.9	1

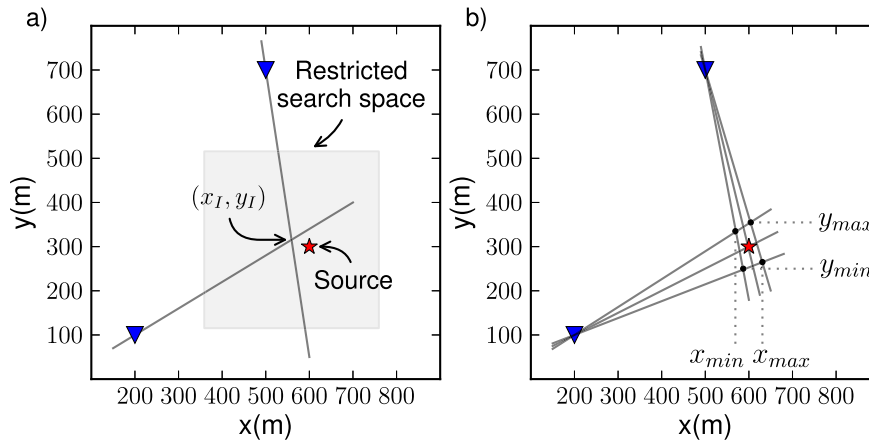


Fig. 7. a) Search space restriction based on backazimuth information. b) Determination of the extent of the search space (see text for details).

for the two wells (Fig. 7a). This would be the case of a velocity model in which only depth variations are considered, such as layered subsurfaces.

A criteria for defining the proper extension of the search space was established from the statistical analysis we describe next. We considered the same set of 400 realizations that correspond to a fictitious source located at $(x_S, y_S, z_S) = (600, 300, 600)$ m. After the detection and denoising, we estimated the corresponding backazimuths for both wells. Table 3 summarizes the resulting means, which are very close to the actual backazimuths, and standard deviations. Assuming that the estimated backazimuths follow a Gaussian distribution, then the probability that θ is within the interval defined by the mean plus minus 3σ is 99%. This range defines a potential region around the intersection point (x_I, y_I) , as shown in Fig. 7b.

For this particular case, $(x_{min}, x_{max}) = (553, 650)$ m and $(y_{min}, y_{max}) = (240, 364)$ m. This analysis can be used to assess the expected variability of the intersection point (and the size of the search space) for a given S/N ratio.

Taking these results into account, in practice for each event we find the intersection point (x_I, y_I) . This point is the center of the search space for the horizontal components. We then set the size of the search space equal to three times the size of the region estimated above. That is, $(x_I \pm 150m, y_I \pm 150m)$. These are the values actually used for the 3D location example. In cases where $\hat{\theta}$ is not reliable or the intersection point is too far from the expected source position, we enlarge the search space so as to encompass the whole stimulated region.

We could follow a similar analysis to restrict the search range for z_S . However, since velocities vary more with depth than with any other direction, the dip information and the corresponding intersection point would not be reliable. For this reason, we prefer to set a wide search range for the depth coordinate. In all the examples considered in this work, we set it equal to $(200, 1000)$ m. A similar approach could be followed for other geometries such as a single deviated monitoring well, or other cases where a 2D location is not possible.

The impact of the search space restriction on the computational cost of the events location process can be assessed by analyzing the results shown in Table 4. The table shows the mean number of cost

function evaluations with a target misfit of 0.5 ms in the cases of the restricted and not-restricted search spaces. The size (in meters) of the horizontal search spaces are 300×300 and 1000×1000 , respectively. As expected, the number of cost function evaluations increases significantly when the search spaces are not restricted, specially for the GS.

4. Conclusions

We implemented an automatic and optimized procedure that concatenates the different steps that lead to the location of the microseismic sources. The detection and denoising method we applied provided the necessary inputs to the backazimuth estimation and location steps, including the energy indicators, that helped to assess the reliability of the detected phase arrivals and avoid possible false detections, and criteria for the identification of the P- and S-waves. In addition, it provided appropriate arrival times and consistent waveforms used for the subsequent steps.

Location involved a non-linear optimization problem where the objective was to minimize the discrepancy between the observed and calculated traveltime differences of the S- and P-waves. We solved this problem by means of two global optimization algorithms: PSO and VFSA. In the 2D location scenario, we searched for two coordinates only, since the backazimuth information that we obtained automatically in a previous step, allowed us to limit the search space to a plane containing the source and the receivers array. In the 3D location scenario the optimization involved three coordinates. For this case, we devised a strategy to restrict the search space based on the backazimuth estimates obtained from two monitoring wells, and showed that this leads to a significant speed-up of calculations. On the other hand, we showed that the proposed energy-based criterion can be used to automatically make the decision whether to use the P- or S-wave backazimuth estimates, an important choice for reliability purposes.

Both PSO and VFSA proved to be very effective and efficient in terms of computational effort when compared against the classical GS, which is used in most commercial software. In this sense, VFSA

Table 3
Actual and mean backazimuth estimates for the set of 400 realizations associated with the same source.

	Well A	Well B
Actual θ	63.43°	165.96°
Mean $\hat{\theta}$	63.40° ± 1.89°	166.34° ± 0.96°

Table 4
Mean number of cost function evaluations (and speed-up) after 400 realizations by restricting or not restricting the search spaces.

	PSO	VFSA	GS
Not restricted	740	385	7758
Restricted	444	243	1910
Speed-up	1.7	1.6	4.1

was up to 8 times faster than GS and 2 times faster than PSO for 3D location. In the 2D case, the speed-ups with respect to GS were about 4 and 2 for VFSA and PSO, respectively. We believe that these speed-ups, together with those obtained by restricting the search space and the energy-based criteria used to select the most reliable backazimuth estimates, might represent a key factor when processing large volumes of data.

Acknowledgments

This work was partially supported by Programa de Incentivos, Universidad Nacional de La Plata (Proyecto 11G135) and Consejo Nacional de Investigaciones Científicas y Técnicas (PIP 112.201201-00626-CO, CONICET), Argentina.

Appendix A. Particle Swarm Optimization (PSO)

PSO is a stochastic optimization technique based on the social and cognitive behavior observed in natural populations such as flocks of birds on their search for food sources (Kennedy and Eberhart, 1995). The algorithm starts with N particles, whose positions represent the model unknowns, randomly distributed throughout the search space. At each iteration their positions are updated based on the corresponding cost function values, weighting both the individual cognition of each particle and the knowledge of the whole group.

Numerous modifications to the method have been applied since its inception, leading to different versions involving diverse parameters (Poli et al., 2007). We next describe the expressions used in this work for the PSO implementation. Let \mathbf{m}_i^k and \mathbf{v}_i^k be the position and velocity of the i -th particle at the k -th iteration and let \mathbf{m}^g be the best position ever reached by a member of the group. Provided the limits of the search space are not exceeded, the velocity at the k -th iteration and the new position at the $(k + 1)$ -th iteration are given by

$$\mathbf{v}_i^k = a \left(\mathbf{v}_i^{k-1} + b\tilde{r} \left(\mathbf{m}_i^l - \mathbf{m}_i^k \right) + c\tilde{r} \left(\mathbf{m}^g - \mathbf{m}_i^k \right) \right), \quad (\text{A.1})$$

$$\mathbf{m}_i^{k+1} = \mathbf{m}_i^k + \mathbf{v}_i^k, \quad (\text{A.2})$$

where \tilde{r} is a random number drawn from a uniform distribution in $[0, 1]$ and $\mathbf{v}_i^0 = 0$ for all particles. The constant a plays the role of a “constriction factor” that helps reducing the velocity magnitudes, which can be quite large depending on the problem. The constants b and c represent the “learning rates” related to the individual cognition and social behavior.

The parameters a , b and c play a key role on the exploration capability of the method, given that they determine the likelihood of a particle to move to other regions of the search space or to concentrate on its

surroundings. The optimum values are those that give the algorithm both behaviors simultaneously and depend on the problem that is being optimized. Previous to this work, we performed a calibration of the algorithm for its use for microseismic event location in order to find the parameters with which it shows better performances in terms of computational efficiency. As a result, we considered $a = 0.4$, $b = 0.8$ and $c = 2.0$. PSO requires one evaluation of the cost function at each iteration and for each particle. Finally, we considered a swarm composed of 50 and 100 particles for the 2D and 3D location, respectively.

References

- Aster, R.C., Barchers, B., Thurber, C.H., 2005. *Parameter Estimation and Inverse Problems*. Elsevier Academic Press.
- Cipolla, C.L., Lewis, R.E., Maxwell, S.C., Mack, M.G., 2011. Appraising unconventional resource plays: separating reservoir quality from completion effectiveness. *International Petroleum Technology Conference*.
- Eisner, L., Duncan, P.M., Heigl, W.M., Keller, W.R., 2009. Uncertainties in passive seismic monitoring. *Lead. Edge* 28, 648–655.
- Eisner, L., Fischer, T., Rutledge, J.T., 2009. Determination of s-wave slowness from a linear array of borehole receivers. *Geophys. J. Int.* 176, 31–39.
- Eisner, L., Hulse, B.J., Duncan, P., Jurick, D., Werner, H., Keller, W., 2010. Comparison of surface and borehole locations of induced seismicity. *Geophys. Prospect.* 58, 809–820.
- Han, L., 2010. *Microseismic Monitoring and Hypocenter Location*. Master's Thesis, University of Calgary.
- Ingber, L., 1989. Very fast simulated re-annealing. *J. Math. Comput. Model.* 12, 967–973.
- Jurkevics, A., 1988. Polarization analysis of three-component array data. *Bull. Seismol. Soc. Am.* 78, 1725–1743.
- Kendall, M., Maxwell, S., Foulger, G., Eisner, L., Lawrence, Z., 2011. Special section. *Microseismicity: beyond dots in a box - introduction*. *Geophysics* 76, WC1–WC3.
- Kennedy, J., Eberhart, R., 1995. Particle swarm optimization. *J. Math. Comput. Model.* 17, 1942–1948.
- Lagos, S.R., Sabbione, J.I., Velis, D.R., 2014. Very fast simulated annealing and particle swarm optimization for microseismic event location. *Expanded Abstracts. Society of Exploration Geophysicists.*, pp. 2188–2192.
- Maxwell, S.C., Rutledge, J., Jones, R., Fehler, M., 2010. Petroleum reservoir characterization using downhole microseismic monitoring. *Geophysics* 75, A129–A137.
- Poli, R., Kennedy, J., Blackwell, T., 2007. Particle swarm optimization: an overview. *Swarm Intell.* 1, 33–57.
- Shaw, R., Srivasta, S., 2007. Particle swarm optimization: a new tool to invert geophysical data. *Geophysics* 72, 75–83.
- Van der Baan, M., Eaton, D., Dusseault, M., 2013. *Microseismic Monitoring Developments in Hydraulic Fracture Stimulation, Effective and Sustainable Hydraulic Fracturing*. Intech.
- Velis, D.R., 1998. *Application of Simulated Annealing to Some Seismic Problems*. Ph.D. Thesis, University of British Columbia, Vancouver, Canada.
- Velis, D.R., Sabbione, J.I., Sacchi, M.D., 2015. Fast and automatic microseismic phase-arrival detection and denoising by pattern recognition and reduced-rank filtering. *Geophysics* 80, WC25–WC38.
- Warpinski, N., 2009. Microseismic monitoring: inside and out. *J. Pet. Technol.* 61, 80–85.
- Zimmer, U., Jin, J., 2011. Fast search algorithms for automatic localization of microseismic events. *CSEG Recorder.*, pp. 40–46.